

Strong, Temperature-Dependent Spin-Orbit Torques in Heavy Fermion YbAl_3

Neal D. Reynolds,^{1,*} Shouvik Chatterjee,^{1,†} Gregory M. Stiehl,¹ Joseph A. Mittelstaedt,¹ Saba Karimeddiny,¹ Alexander J. Buser,¹ Darrell G. Schlom,^{2,3} Kyle M. Shen,^{1,3} and Daniel C. Ralph^{1,3}

¹*Department of Physics, Cornell University, Ithaca, NY 14853, USA*

²*Department of Materials Science and Engineering, Cornell University, Ithaca, NY 14853, USA*

³*Kavli Institute at Cornell, Cornell University, Ithaca, NY 14853, USA*

(Dated: March 2, 2022)

The use of current-generated spin-orbit torques¹ to drive magnetization dynamics is under investigation to enable a new generation of non-volatile, low-power magnetic memory. Previous research has focused on spin-orbit torques generated by heavy metals^{2–8}, interfaces with strong Rashba interactions^{9,10} and topological insulators^{11–14}. These families of materials can all be well-described using models with noninteracting-electron bandstructures. Here, we show that electronic interactions within a strongly correlated heavy fermion material, the Kondo lattice system YbAl_3 , can provide a large enhancement in spin-orbit torque. The spin-torque conductivity increases by approximately a factor of 4.5 as a function of decreasing temperature from room temperature to the coherence temperature of YbAl_3 ($T^* \approx 37$ K), with a saturation at lower temperatures, achieving a maximum value greater than any heavy metal element. This temperature dependence mimics the increase and saturation at T^* of the density of states at the Fermi level arising from the ytterbium 4*f*-derived heavy bands in the Kondo regime, as measured by angle-resolved photoemission spectroscopy¹⁵. We therefore identify the many-body Kondo resonance as the source of the large enhancement of spin-orbit torque in YbAl_3 . Our observation reveals new opportunities in spin-orbit torque manipulation of magnetic memories by engineering quantum many-body states.

Research on materials that can be used to generate strong spin-orbit torques has focused primarily on elements, alloys and compounds containing *d*-electrons, with a few exceptions^{16–21}. In *d*-electron materials, inter-atom coupling produces electronic bands with relatively large bandwidths, such that effective independent-electron models provide a reasonable description of most electronic properties. In *f*-electron materials, by comparison, the electron bandwidths are narrower and electronic interactions can be much more impactful, increasing the potential importance of electron correlations. For the pure *f*-electron metals measured to date, the *f*-electron

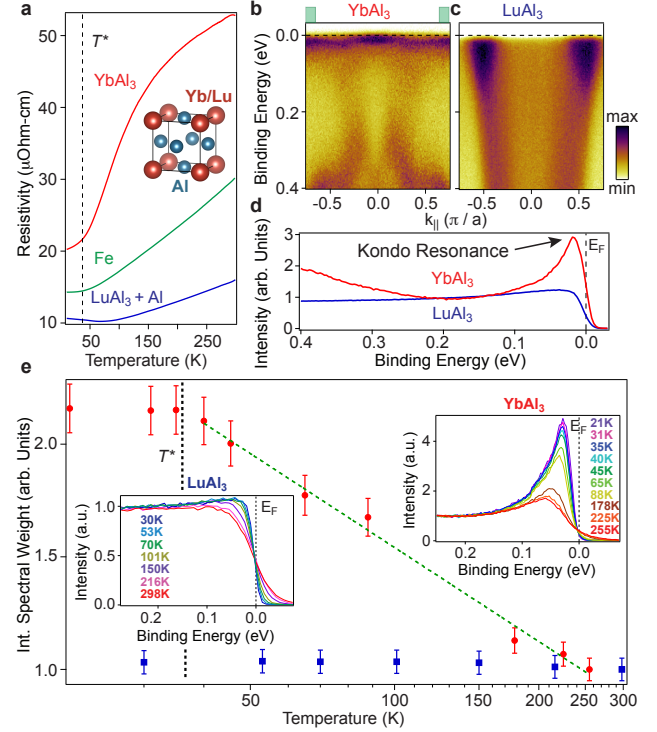


FIG. 1. Transport and spectroscopy of YbAl_3 and LuAl_3 thin films. **a**, Temperature-dependent resistivities of YbAl_3 , $\text{LuAl}_3 + \text{Al}$, and Fe. The dashed line indicates the coherence temperature of YbAl_3 ($T^* = 37$ K) below which its resistivity exhibits a Fermi-liquid behavior, $\rho \propto T^2$. Inset: Crystal structure of YbAl_3 and LuAl_3 . **b,c**, Measured E - k spectral maps at 21 K along $(0,0) - (0,\pi)$ near the bulk Γ point for (b) YbAl_3 and (c) LuAl_3 . **d**, Energy distribution curves obtained from spectral maps in (b) and (c) by integrating over in-plane momenta between $-0.5\pi/a$ and $0.5\pi/a$. **e**, Spectral weight integrated over $-0.05 - 0.2$ eV binding energy for (red circles) YbAl_3 and (blue squares) LuAl_3 . Integrated spectral weight in YbAl_3 is obtained from energy distribution curves integrated over a momentum region $\pm(0.66 - 0.75 \pi/a)$ shown in green in **b**, after subtracting an inelastic background. The green dashed line illustrates a scaling $\propto \ln(T_0/T)$ between 250 K and 37 K. Insets: momentum-integrated energy distribution curves (EDCs) at different sample temperatures for YbAl_3 and LuAl_3 .

* ndr37@cornell.edu; equal contribution

† equal contribution

density of states at the Fermi level happens to be negligible (the dominant contribution to the electronic density of states near E_F is from the *d* orbitals), and hence the

effects of electron correlations on the spin-orbit torques from these materials are expected to be only modest²⁰. Still, previous studies of pure *f*-electron elements have measured enhancements in spin-orbit torque due to a contribution from *f*-electron bands^{18–20}, with a maximum spin-torque conductivity at room temperature of $2 \times 10^4 \frac{\hbar}{2e} \Omega^{-1} \text{m}^{-1}$ for Ho²⁰. Spin-orbit torques strong enough to switch magnetic layers have been observed in the *f*-electron-containing topological Kondo insulator candidate SmB₆²¹, but the role of strong correlations or the contribution of the *f*-electronic density of states was not clear.

To probe whether correlated electron effects in *f*-electron materials can enhance spin-orbit torques, we investigated the Kondo lattice system YbAl₃. YbAl₃ has a relatively high Kondo temperature of ≈ 670 K, the energy scale for the Kondo interaction between the localized Yb 4*f* moments and the delocalized conduction electrons leading to the formation of a Kondo screened many-body state of predominantly Yb 4*f* character^{22,23}. This Kondo effect generates a narrow Yb 4*f*-derived band close to the Fermi level that is prominent in angle-resolved photoemission spectroscopy (ARPES) measurements¹⁵ as shown in Fig. 1b, 1d. Near the Fermi energy, the integrated spectral weight averaged over a region of momentum space away from the electron pocket centered at $k_{\parallel}=0$ [*i.e.* the momentum region where only the Yb-4*f*-derived Kondo band is present (see Methods)] grows approximately logarithmically with decreasing temperature from 250 K down to the coherence temperature ($T^* \approx 37$ K) (Fig. 1e), and saturates at lower temperatures where YbAl₃ exhibits Fermi liquid behavior. This observation is in accord with expectations from a phenomenological two-fluid model, as has also been seen in other Kondo lattice systems^{24–26}.

Here, we report measurements of the strength of spin-orbit torque produced by YbAl₃ as a function of temperature to study whether the presence of the Kondo-induced 4*f*-derived heavy band near the Fermi level can enhance the spin-torque efficiency. In order to distinguish the influence of the emergent 4*f*-derived heavy quasi particles on spin-orbit torque generation in YbAl₃ from the contributions of other *d*, *p*, and *s* derived bands, we also examined control samples of LuAl₃, which has a similar crystal structure and lattice constants as YbAl₃, but in which the Kondo interaction is absent due to the fully-filled 4*f* shell of the Lu³⁺ ions. Therefore, unlike in YbAl₃, only wide bands predominantly of Al *p* orbital character cross the Fermi level in LuAl₃ (Fig. 1c), with negligible temperature dependence for the integrated spectral weight (Fig. 1e).

To measure the spin-orbit torque generation in these compounds, we fabricated heterostructures in which epitaxial layers of ferromagnetic Fe were grown on single crystal epitaxial layers of YbAl₃ or LuAl₃. The growth was performed by molecular-beam epitaxy on MgO substrates as described in Methods and in ref.²⁷. To obtain high quality heterostructures, atomic layers of YbAl₃

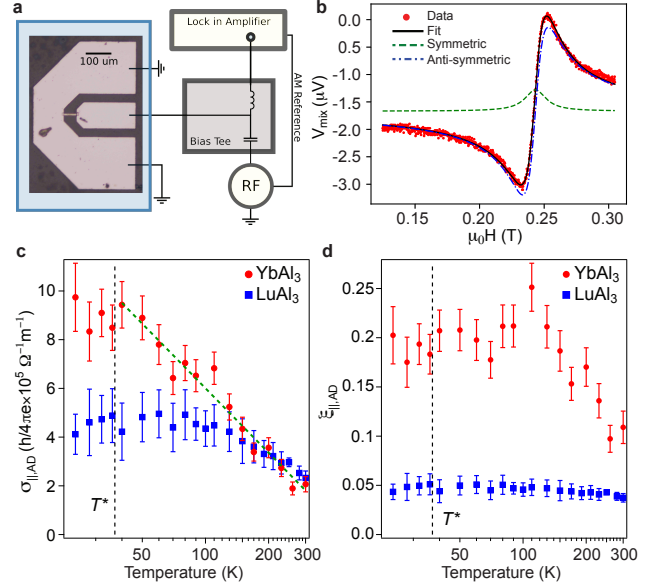


FIG. 2. ST-FMR measurements of current-induced torque in a 1.8 nm Al/5 nm LuAl₃/6.7 nm YbAl₃/6 nm Fe/ oxidized Al heterostructure. **a**, Schematic of the ST-FMR measurement setup. **b**, Representative DC mixing voltage trace taken at 40 K at a frequency $f = 22$ GHz. The black line is a fit to Eq. (1) (see Methods), with the symmetric Lorentzian and antisymmetric Lorentzian components shown in green and blue dot-dash lines, respectively. **c**, Spin-orbit-torque conductivity and **d**, spin-torque ratio determined via ST-FMR. The green dashed line in (c) is a guide to the eye for $\ln(\frac{T_0}{T})$ temperature scaling.

were first deposited on buffer layers containing 1.8 nm thick Al and 5 nm thick LuAl₃ atomic layers. The samples analyzed in this paper for spin-torque measurements contained 1.8 nm Al, 5 nm LuAl₃ (6.7, 15, 18) nm YbAl₃ and 6 nm Fe, while the control samples consisted of 1.8 nm Al, 15 nm LuAl₃ and 6 nm Fe. All samples were capped with 3 nm of Al, which oxidizes to form a protective layer of AlO_x upon exposure to atmosphere. The temperature-dependent resistivities of the YbAl₃, LuAl₃ + Al and Fe atomic layers, extracted from the full heterostructures (Supplementary Information), are shown in Fig. 1a. For spin-torque measurements, the films were patterned using optical lithography and ion milling into simple wires 6–60 μm wide and 40–80 μm long, and then Ti/Pt electrical contacts were deposited. (The device geometry is shown in Fig. 2a.)

We performed quantitative measurements of the spin-orbit torques generated by YbAl₃ and LuAl₃ by detecting the deflection of the magnetization of the Fe layer in response to charge currents applied in the plane of the heterostructure. We read out this deflection in two independent ways: electrically via the spin-torque ferromagnetic resonance (ST-FMR) technique^{3,11} and optically using the magneto-optical Kerr effect (MOKE)²⁸. We performed ST-FMR on samples with all three thick-

nesses of YbAl₃, observing quantitatively similar behavior.

For ST-FMR, we applied a $f = 18\text{--}23$ GHz oscillating drive current in the presence of a swept external magnetic field at a fixed in-plane angle that orients the equilibrium direction of the Fe magnetization at an angle ϕ with respect to the current flow direction. As the field is swept through the resonance condition of the magnetic layer, the magnetization is driven into ferromagnetic resonance. The resulting precessional motion of the magnetization near resonance gives rise to an oscillating longitudinal resistance through the magnet's anisotropic magnetoresistance (AMR). The mixing of this resistance oscillation and driving signal results in a DC voltage signal, V_{mix} , that has the form of a sum of an anti-symmetric and a symmetric Lorentzian. Figure 2b shows a representative resonance at 40 K for a driving frequency of 22 GHz at $\phi = 45^\circ$ with respect to the current flow direction, along with fits. From the magnitudes of the antisymmetric and the symmetric Lorentzians we extract the out-of-plane torque (τ_\perp) and the in-plane torque (τ_\parallel), respectively. By varying the angle at which the external field is applied, we determined the symmetries of the torques that make up τ_\perp and τ_\parallel . The component of primary interest is the in-plane antidamping torque $\tau_{\parallel,AD}$, which varies $\propto \cos(\phi_B)$. For details of the analysis, see Methods.

Figures 2c,d show two ways of quantifying the measured strength of the in-plane antidamping spin-orbit torques generated by YbAl₃ and LuAl₃ as determined by ST-FMR. Figure 2c displays the spin-orbit-torque conductivities $\sigma_{\parallel,AD}$, equal to the maximum transverse angular momentum density absorbed by the magnetic layer per unit applied electric field. Figure 2d shows the dimensionless spin-orbit-torque ratios per unit applied charge current density in the spin-orbit source material $\xi_{\parallel,AD} = \frac{\hbar}{2e} \frac{\sigma_{\parallel,AD}}{\sigma}$, where σ is the charge conductivity in the spin-orbit source layer. These quantities should be considered as lower bounds for the internal spin Hall conductivity and internal spin Hall ratio within the spin-orbit source material, as they are reduced by an interfacial transmission factor for the spin current to be absorbed by the magnetic layer.

For the control sample in which LuAl₃ is the spin-orbit source layer, we find that $\sigma_{\parallel,AD, \text{LuAl}_3}$ increases only moderately from $(2.3 \pm 0.3) \times 10^5 \frac{\hbar}{2e} \Omega^{-1} \text{ m}^{-1}$ at 300 K to $(5.0 \pm 1.0) \times 10^5 \frac{\hbar}{2e} \Omega^{-1} \text{ m}^{-1}$ below 90 K, while $\xi_{\parallel,AD, \text{LuAl}_3} \approx 0.04$ and is approximately constant as a function of temperature. This type of weak temperature dependence is similar to previous measurements of antidamping spin-orbit torque generated by the intrinsic spin Hall effect in d -electron heavy metals^{29–31}. In contrast, the spin-orbit torque from YbAl₃ has a much more dramatic temperature dependence. At room temperature, $\sigma_{\parallel,AD, \text{YbAl}_3} = (2.1 \pm 0.3) \times 10^5 \frac{\hbar}{2e} \Omega^{-1} \text{ m}^{-1}$, comparable to $\sigma_{\parallel,AD, \text{LuAl}_3}$, but with decreasing temperature $\sigma_{\parallel,AD, \text{YbAl}_3}$ increases approximately logarithmically to a value of $(9.4 \pm 1.0) \times 10^5 \frac{\hbar}{2e} \Omega^{-1} \text{ m}^{-1}$ before appearing to saturate below 40 K, roughly the coherence tempera-

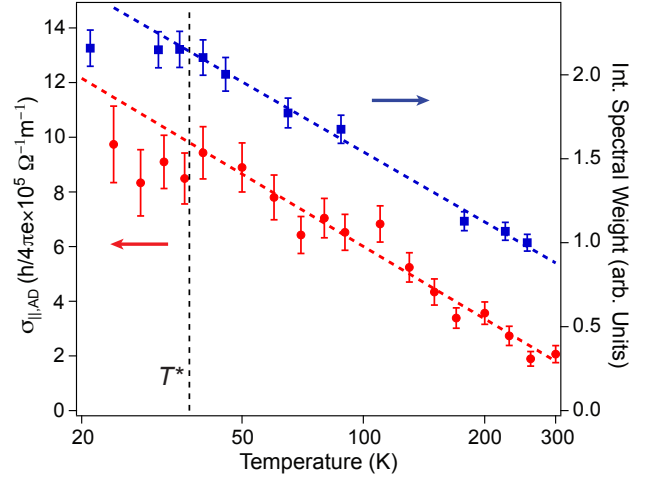


FIG. 3. **Scaling comparison of $\sigma_{\parallel,AD}$ and YbAl₃ $4f$ spectral weight with temperature.** $\sigma_{\parallel,AD}$ (red circles, left axis) is compared to the integrated $4f$ spectral weight (blue squares, right axis). The vertical dashed line highlights the coherence temperature $T^* = 37$ K of YbAl₃. The colored, parallel dashed lines are guides to the eye $\propto \ln(T_0/T)$.

ture of YbAl₃ discussed above. Correspondingly, the spin torque ratio $\xi_{\parallel,AD, \text{YbAl}_3}$ is also strongly temperature-dependent and grows much larger than the value for LuAl₃.

The dramatic logarithmic temperature dependence for the antidamping spin-orbit-torque conductivity, an enhancement of $\sigma_{\parallel,AD}$ by approximately a factor of 4.5 compared to the room temperature value, is quite unusual. In heavy metals, the spin-orbit torque varies at most about 10% from room to cryogenic temperatures^{30,31}. As far as we are aware, the only strong temperature dependencies observed previously for $\sigma_{\parallel,AD}$ in spin-orbit-torque metals are in ferromagnetic alloys, which can exhibit approximately a factor of 4 enhancement near their Curie temperature due to scattering from magnetic fluctuations³² and in high-resistivity SrRuO₃ which shows a factor of 8 enhancement with decreasing temperature associated with the variation in carrier lifetime in the bad-metal regime^{33,34}. Neither of these mechanisms is applicable to YbAl₃, since it does not undergo a magnetic phase transition and it has a low resistivity ($< 50 \mu\Omega\text{-cm}$, see Fig. 1a) over the entire temperature range we consider. The maximum values of $\sigma_{\parallel,AD}$ for YbAl₃ near T^* , $(9.4 \pm 1.0) \times 10^5 \frac{\hbar}{2e} \Omega^{-1} \text{ m}^{-1}$, is strikingly large – larger than reported for any heavy metal. It is surpassed in the literature only by topological insulators such as $(\text{Bi}_{0.5}\text{Sb}_{0.5})_2\text{Te}_3$ and $\text{Bi}_{0.9}\text{Sb}_{0.1}$ ^{12,13}.

We have verified these results independently by using MOKE to measure the current-induced magnetization tilt in YbAl₃/Fe samples. The temperature stability of the optical cryostat limits our MOKE results to below 77 K, but in this range the MOKE results confirm the very large values of antidamping spin-orbit torque conductiv-

ity (see Supplementary Information).

A comparison between the temperature dependence of the integrated spectral weight measured by ARPES and the spin torque conductivity $\sigma_{\parallel,AD}$ is shown in Fig.3. Both quantities increase with decreasing temperature with approximately a $\log \frac{T_0}{T}$ scaling between room temperature and the coherence temperature, $T^* = 37$ K. Below this temperature, both quantities saturate. The measured enhancement in the integrated spectral weight ranges between a factor of approximately 2 and 4 depending on the integration window and the background subtraction (see Supplementary Information). The factor of 4.5 enhancement in the spin torque conductivity is quite comparable, considering that the contribution to $\sigma_{\parallel,AD}$ from different electronic bands will depend on factors like Berry curvature as well as spectral weight.

ARPES measurements have identified the temperature-dependent changes in the electronic structure of YbAl₃ as due to increasing hybridization between Yb 4*f* local moments and delocalized conduction electrons, resulting in the formation of Kondo screened many-body states. Based on the similarities in the logarithmic temperature scaling and saturation below T^* , we identify the large enhancement in spin-torque conductivity as due to the same many-body Kondo effect. Our observations are qualitatively consistent with predictions in ref.²⁰ that the enhancement in spin-orbit torque can be achieved by increasing hybridization of the 4*f* states into the itinerant bands near the Fermi level. The strong enhancement that we measure of the spin-orbit torque associated with the Kondo effect in YbAl₃ suggests that engineering of many-body states in correlated electron systems (particular those containing partially filled *f* shells) can be a productive strategy for increasing the efficiency of spin-orbit torques. The same sensitivity may also enable spin-orbit torques to be a useful new tool for characterizing heavy fermion systems.

I. ACKNOWLEDGEMENTS

Primary support for this work was provided by the National Science Foundation (DMR-1708499 and DMR-1709255), and by the Gordon and Betty Moore Foundation as part of the EPiQS initiative (GBMF3850). Additional support was provided by the NSF MRSEC program through the Cornell Center for Materials Research (DMR-1719875). This work was performed in part at the Cornell NanoScale Facility, an NNCI member supported by the NSF (NNCI-1542081) and at the Cornell Center for Materials Research shared facilities.

II. METHODS

A. Thin Film Growth

Single crystalline, epitaxial YbAl₃ thin films were synthesized on MgO (001) substrates using a Veeco Gen10 molecular-beam epitaxy (MBE) system with base pressure better than 2×10^{-9} Torr. Prior to growth, the MgO substrates were annealed in vacuum for 20 min at 800°C. A 1.8 nm thick aluminum (Al) buffer layer was deposited at 500°C followed by a 5 nm thick LuAl₃ layer on which YbAl₃ layers were synthesized. Al and LuAl₃ buffer layers were found to be essential for the synthesis of high quality YbAl₃ thin films. For the growth of LuAl₃ and YbAl₃ layers, Lu/Yb and Al were co-evaporated from effusion cells at a rate of ≈ 0.4 nm/min onto a rotating substrate with real-time reflection high-energy electron diffraction (RHEED) monitoring. The LuAl₃ atomic layers were deposited at 200°C and annealed at 350°C for 30 min, following which YbAl₃ deposition was initiated at 200°C and ramped up to 315°C during growth. Due to the co-evaporation method, the surface termination was not deliberately controlled. Fe layers were deposited either on LuAl₃ or on YbAl₃ layers at 200°C followed by the deposition of a 3 nm thick Al capping layer at room temperature to prevent oxidation of the underlying heterostructure. Further details about the thin film growth and characterization of the heterostructure can be found in the Supplementary Information and in ref.²⁷

B. Magnetic Characterization

The sample saturation magnetization, M_s , was determined using the vibrating sample magnetometry (VSM) option of a Quantum Design physical properties measurement system (PPMS) using a portion of the remaining un-patterned film after fabrication. We find an M_s which varies between a maximum of 1.42×10^6 A/m at 290 K to a minimum of 1.24×10^6 A/m at 70 K which then recovers to 1.38×10^6 A/m at 20 K. The changes appear to follow the magnetic susceptibility of YbAl₃³⁵ (times a minus sign), suggesting a proximity effect in which a small induced moment in YbAl₃ is antiparallel to that in the Fe layer. The cubic magnetocrystalline anisotropy field H_a and sample effective magnetization M_{eff} were extracted from ST-FMR measurements of the resonance field as a function of the angle of the applied magnetic field assuming tetragonal magnetocrystalline anisotropy³⁶. We determined that magnetic easy axes lie along the YbAl₃ (110) directions (these are the Fe (100) directions), and that the anisotropy field H_a increases monotonically with decreasing temperature from a room temperature value of 0.58 T to 0.78 T at 20 K. We find that M_{eff} has a larger magnitude than M_s and monotonically increases with decreasing temperature from a value of 1.95×10^6 A/m to 2.04×10^6 A/m at 40 K. (Plots of M_s , H_a , M_{eff} , as well as the explicit forms of the resonance field angular

dependence used to find H_a and M_{eff} may be found in the Supplementary Information.)

C. Angle-resolved Photoemission Spectroscopy

Angle-resolved Photoemission Spectroscopy was performed using He I α photons from a VUV500 helium plasma discharge lamp in a measurement chamber with base pressure better than 5×10^{-11} Torr and equipped with a VG Scienta R4000 electron analyzer. Samples were transferred from the growth chamber into the measurement chamber under ultra-high vacuum conditions immediately after the completion of the growth process. To extract the integrated spectral weight shown in Fig. 1e, energy distribution curves were obtained by integrating along the Γ -X direction over a momentum region $\pm(0.66 - 0.75) \pi/a$, for a value of k_z close to the bulk Γ point. An inelastic background was then subtracted. Further details about the background subtraction can be found in the Supplementary Information.

D. Spin-Torque Ferromagnetic Resonance (ST-FMR)

We perform ST-FMR measurements using a radio frequency (RF) insert within a sample-in-vapor He flow cryostat. A semi-rigid coaxial line is terminated in a coplanar waveguide to which we wirebond our device in a ground-signal-ground configuration. We apply a 18-23 GHz RF current to the device in the presence of a swept magnetic field at an angle ϕ_B with respect to the current flow direction. For the data shown in the main text, current flows along the YbAl $_3$ [100] direction. The magnetic field is provided by an external electromagnet mounted on a motorized base. Due to the relatively strong tetragonal magnetic anisotropy, the magnetization angle ϕ is generally slightly misaligned with ϕ_B . We perform fits relative to the actual magnetization angle ϕ rather than ϕ_B , calculating ϕ based on the measured anisotropy and the applied field strength. Current-driven precession of the magnetization results in an oscillation of the longitudinal resistance of the device through the Fe layer's anisotropic magnetoresistance. The in-phase component of this resistance oscillation mixes with the RF current to create a DC voltage V_{mix} across the device given within a macrospin approximation by³:

$$V_{\text{mix}} \approx \frac{(R_{\parallel} - R_{\perp}) \sin(\phi) \cos(\phi) I_0 \omega \tau_0}{\gamma^2 \Delta (2B_0 + \mu_0 M_{\text{eff}})} \times \left[S(\phi) F_S(B) + \sqrt{1 + \frac{\mu_0 M_{\text{eff}}}{B_0}} A(\phi) F_A(B) \right] \quad (1)$$

where $(R_{\parallel} - R_{\perp})$ is the difference in device resistance with the magnetization parallel and perpendicular to the current flow direction; I_0 is the RF current reaching the device; ω is the frequency of the driving current;

$\tau_0 \equiv \gamma \frac{\hbar}{2e} \frac{J_{c,YbAl_3}}{M_s t_{\text{mag}}}$; $J_{c,YbAl_3}$ is the charge current density flowing within the YbAl $_3$ layer; M_s is the saturation magnetization of the Fe layer; t_{mag} is the thickness of the magnetic layer; Δ is the resonance linewidth as a function of magnetic field; B_0 is the resonant field; M_{eff} is the effective magnetization; $F_S(B) = \frac{\Delta^2}{(B-B_0)^2 + \Delta^2}$ is a symmetric Lorentzian; and $F_A(B) = \frac{B-B_0}{\Delta} F_S(B)$ is an antisymmetric Lorentzian.

We fit the amplitude of the symmetric component, containing information on the in-plane (IP) torques, to the form

$$S(\phi) \equiv \cos(\phi) \xi_{\parallel,AD} + \xi_{\parallel,0}. \quad (2)$$

The term $\xi_{\parallel,0}$ is included to account for any torque due to an out-of-plane Oersted field that can result from unequal current flow in the two branches of the ground-signal-ground contact geometry (e.g., due to different wirebond impedance; this term is always small relative to $\xi_{\parallel,AD}$). We fit the amplitude of the anti-symmetric Lorentzian, containing information on the out-of-plane (OOP) torques to the form

$$A(\phi) \equiv \cos(\phi) (\xi_{\perp,FL} + \xi_{Oe}), \quad (3)$$

accounting for contributions from an OOP field-like spin-orbit torque and the torque due to the in-plane Oersted field generated by current flowing within the plane of the heterostructure:

$$\xi_{Oe} \equiv \frac{\gamma \mu_0 (J_{c,YbAl_3} t_{Yb_3} + J_{c,LuAl_3+Al} t_{LuAl_3+Al})}{2\tau_0}. \quad (4)$$

Note that this definition accounts for the fact that current density in the LuAl $_3$ and Al seed layers contribute to the Oersted field torque, despite the fact that Eq. (1) is defined in terms of the current density through the YbAl $_3$ layer only. The antidamping spin-orbit torque conductivity is $\sigma_{\parallel,AD} = \xi_{\parallel,AD} \times \sigma$, where σ is the charge conductivity of the YbAl $_3$ layer.

One challenging part of the analysis is calibrating the magnitude of the applied microwave current that reaches the device, I_0 . The wirebonds make it difficult to measure the microwave transmission coefficients accurately using a vector network analyzer. Instead, we utilize a variation on the thermal power calibration method described in ref.³⁷. We measure the device resistance, R , as a function of applied DC bias, I_{DC} , from -10 mA to 10 mA and confirm the expected I_{DC}^2 dependence of R . We then apply 0 dBm to 20 dBm of RF power at a given frequency to the device in addition to a 500 μ A DC sensing current to the device to extract the RF power dependence of R . Because all of the DC bias current reaches the device, we can then compare the slopes of the device resistance vs total power applied to the device for both the DC bias and RF bias to extract the fraction of RF power which reaches the device. We do this for frequencies from 15-23 GHz at temperature from 20-300 K to map out the scattering parameters of our cryostat and

device thus allowing us to calculate I_0 for our devices. To verify the accuracy of this analysis, we compare our thermal power calibration scattering parameters to vector network analyzer derived values on our probe station which is not confounded by the problem of wirebonds.

A second challenging aspect of the analysis is that in measurements of V_{mix} versus ϕ we can observe deviations from the expected dependence in Eq. (1) near $\phi \approx 0^\circ$ and 180° , the two magnetic hard axes where the current-induced torques are strong. We ascribe these deviations to non-macrospin dynamics near these hard axes. Quantitative measurements can still be obtained by focusing on measurements near the easy axes $\phi = \pm 45^\circ, \pm 135^\circ$, or by adding a correction factor to the angular fits as discussed in the Supplementary Information.

III. AUTHOR INFORMATION

SC, NDR, KMS and DCR conceived of the experiment. SC grew and characterized the sample films. NDR fabricated the devices and built the angle-resolved cryo-ST-FMR apparatus. NDR acquired the ST-FMR, MOKE and magnetometry data with help from JAM, SK, and AJB. SC acquired the ARPES data. NDR and SC analyzed the data with help from GMS, DCR, KMS and DGS. SC, NDR, DGS, KMS and DCR wrote the manuscript and all authors contributed to the final version.

-
- [1] Sinova, J., Valenzuela, S. O., Wunderlich, J., Back, C. & Jungwirth, T. Spin Hall effects. *Rev. Mod. Phys.* **87**, 1213–1260 (2015).
 - [2] Ando, K. *et al.* Electric manipulation of spin relaxation using the spin Hall effect. *Phys. Rev. Lett.* **101**, 036601 (2008).
 - [3] Liu, L., Moriyama, T., Ralph, D. C. & Buhrman, R. A. Spin-torque ferromagnetic resonance induced by the spin Hall effect. *Phys. Rev. Lett.* **106**, 036601 (2011).
 - [4] Miron, I. M. *et al.* Perpendicular switching of a single ferromagnetic layer induced by in-plane current injection. *Nature* **476**, 189 (2011).
 - [5] Liu, L. *et al.* Spin-torque switching with the giant spin Hall effect of tantalum. *Science* **336**, 555–558 (2012).
 - [6] Pai, C.-F. *et al.* Spin transfer torque devices utilizing the giant spin Hall effect of tungsten. *Appl. Phys. Lett.* **101**, 122404 (2012).
 - [7] Emori, S., Bauer, U., Ahn, S.-M., Martinez, E. & Beach, G. S. Current-driven dynamics of chiral ferromagnetic domain walls. *Nat. Mater.* **12**, 611–616 (2013).
 - [8] Ryu, K.-S., Thomas, L., Yang, S.-H. & Parkin, S. Chiral spin torque at magnetic domain walls. *Nat. Nanotechnol.* **8**, 527–533 (2013).
 - [9] Jungfleisch, M. *et al.* Interface-driven spin-torque ferromagnetic resonance by Rashba coupling at the interface between nonmagnetic materials. *Phys. Rev. B* **93**, 224419 (2016).
 - [10] Yue, D., Lin, W., Li, J., Jin, X. & Chien, C. Spin-to-charge conversion in Bi films and Bi/Ag bilayers. *Phys. Rev. Lett.* **121**, 037201 (2018).
 - [11] Mellnik, A. *et al.* Spin-transfer torque generated by a topological insulator. *Nature* **511**, 449–451 (2014).
 - [12] Fan, Y. *et al.* Magnetization switching through giant spin-orbit torque in a magnetically doped topological insulator heterostructure. *Nat. Mater.* **13**, 699 (2014).
 - [13] Khang, N. H. D., Ueda, Y. & Hai, P. N. A conductive topological insulator with large spin Hall effect for ultralow power spin-orbit torque switching. *Nat. Mater.* **17**, 808–813 (2018).
 - [14] Mahendra, D. *et al.* Room-temperature high spin-orbit torque due to quantum confinement in sputtered $\text{Bi}_x\text{Se}_{1-x}$ films. *Nat. Mater.* **17**, 800–807 (2018).
 - [15] Chatterjee, S. *et al.* Lifshitz transition from valence fluctuations in YbAl_3 . *Nat. Commun.* **8** (2017).
 - [16] Tanaka, T. & Kontani, H. Giant extrinsic spin Hall effect due to rare-earth impurities. *New J. Phys.* **11**, 013023 (2009).
 - [17] Tanaka, T. & Kontani, H. Intrinsic spin and orbital Hall effects in heavy-fermion systems. *Phys. Rev. B* **81**, 224401 (2010).
 - [18] Singh, S., Anguera, M., del Barco, E., Springell, R. & Miller, C. W. Moderate positive spin Hall angle in uranium. *Appl. Phys. Lett.* **107**, 232403 (2015).
 - [19] Ueda, K., Pai, C.-F., Tan, A. J., Mann, M. & Beach, G. S. Effect of rare earth metal on the spin-orbit torque in magnetic heterostructures. *Appl. Phys. Lett.* **108**, 232405 (2016).
 - [20] Reynolds, N. *et al.* Spin Hall torques generated by rare-earth thin films. *Phys. Rev. B* **95**, 064412 (2017).
 - [21] Li, Y., Ma, Q., Huang, S. & Chien, C. Thin films of topological Kondo insulator candidate SmB_6 : Strong spin-orbit torque without exclusive surface conduction. *Sci. Adv.* **4**, eaap8294 (2018).
 - [22] Cornelius, A. *et al.* Two energy scales and slow crossover in YbAl_3 . *Phys. Rev. Lett.* **88**, 117201 (2002).
 - [23] Ebihara, T. *et al.* Dependence of the Effective Masses in YbAl_3 on Magnetic Field and Disorder. *Phys. Rev. Lett.* **90**, 166404 (2003).
 - [24] Choi, H. C., Min, B., Shim, J., Haule, K. & Kotliar, G. Temperature-dependent Fermi surface evolution in heavy fermion CeIrIn_5 . *Phys. Rev. Lett.* **108**, 016402 (2012).
 - [25] Yang, Y.-f. & Pines, D. Universal behavior in heavy-electron materials. *Phys. Rev. Lett.* **100**, 096404 (2008).
 - [26] Yang, Y.-f. & Pines, D. Emergent states in heavy-electron materials. *Proc. Natl. Acad. Sci.* **109**, E3060–E3066 (2012).
 - [27] Chatterjee, S. *et al.* Epitaxial growth and electronic properties of mixed valence YbAl_3 thin films. *J. Appl. Phys.* **120**, 035105 (2016).
 - [28] Fan, X. *et al.* Quantifying interface and bulk contributions to spin-orbit torque in magnetic bilayers. *Nat. Comm.* **5**, 3042 (2014).
 - [29] Kim, J. *et al.* Anomalous temperature dependence of current-induced torques in CoFeB/MgO heterostructures with Ta-based underlayers. *Phys. Rev. B* **89**, 174424 (2014).

- (2014).
- [30] Qiu, X. *et al.* Angular and temperature dependence of current induced spin-orbit effective fields in Ta/CoFeB/MgO nanowires. *Sci. Rep.* **4**, 4491 (2014).
 - [31] Ou, Y., Pai, C.-F., Shi, S., Ralph, D. & Buhrman, R. Origin of fieldlike spin-orbit torques in heavy metal/ferromagnet/oxide thin film heterostructures. *Phys. Rev. B* **94**, 140414 (2016).
 - [32] Ou, Y., Ralph, D. & Buhrman, R. Strong enhancement of the spin Hall effect by spin fluctuations near the Curie point of $\text{Fe}_x\text{Pt}_{1-x}$ alloys. *Phys. Rev. Lett.* **120**, 097203 (2018).
 - [33] Ou, Y. *et al.* Exceptionally high, strongly temperature dependent, spin Hall conductivity of SrRuO_3 . *Nano Lett.* **19**, 3663–3670 (2019).
 - [34] Tanaka, T. *et al.* Intrinsic spin hall effect and orbital hall effect in 4 d and 5 d transition metals. *Physical Review B* **77**, 165117 (2008).
 - [35] Hiess, A., Boucherle, J., Givord, F. & Canfield, P. Magnetic susceptibility and magnetization measurements of an YbAl_3 single crystal for groundstate investigations. *J. Alloys Compd.* **224**, 33–35 (1995).
 - [36] Farle, M. Ferromagnetic resonance of ultrathin metallic layers. *Rep. Prog. Phys.* **61**, 755 (1998).
 - [37] Tshitoyan, V. *et al.* Electrical manipulation of ferromagnetic NiFe by antiferromagnetic IrMn. *Phys. Rev. B* **92**, 214406 (2015).